

Magnetic current imaging with magnetic tunnel junction sensors: case study and analysis

Benaiah D. Schrag, Matthew J. Carter, Xiaoyong Liu, Jan S. Hoftun, and Gang Xiao
Micro Magnetics, Inc., Fall River, MA, USA

Abstract

We describe the use of magnetic tunnel junction (MTJ) sensors for the purposes of magnetic current imaging. First, a case study shows how magnetic and current density images generated using an MTJ sensor probe were used to isolate the root cause of failure in a newly-designed ASIC. We then give a brief introduction to the operation and construction of MTJ sensors. Finally, a full comparison is made between the three types of sensors which have been used for magnetic current imaging: giant magnetoresistive (GMR) sensors, superconducting quantum interference devices (SQUIDs), and magnetic tunnel junctions. These three technologies are quantitatively compared on the basis of spatial resolution, sensitivity, and geometry.

Case Study: Introduction

A small fabless design house was looking for quick fault isolation and failure analysis on an ASIC they were developing. They had limited in-house resources and wanted to quickly correct any errors and get a working device to the market. The ASIC, which contained analog and digital sections, was a low-power, precision power monitoring and conditioning device with a communication bus allowing ganged operation of many units. The entire lot of die from the first shuttle run of the device was found to be non-functional. All the die exhibited shorts of some kind, though the exact mechanism(s) involved differed from chip to chip.

Initial inspection using a test evaluation board showed excessive supply currents, clamped output voltages, and non-functional logic. The test board was designed to allow the ASIC to be power cycled, voltages ramped, logic tested and the outputs monitored. Per its design, the ASIC should have drawn on the order of 10 μ A from the supply, but the actual devices had supply currents greater than 1 mA. In no device tested did the digital block exhibit a logic response of any kind. Some die had shorts between the voltage regulator (VLDO) and the battery ground (VBAT0) pins, some had VLDO to battery voltage (VBAT1) shorts, and others had both. Due to the varied fault modes it was initially thought that a design rule might have been violated. However, design check, layout check, and database check found no such violations.

The first technique used for analysis was liquid crystal. The technique seemed to indicate excessive joule heating in the digital block of the ASIC. However, the amount of power

dissipated was so great that the area darkened by the liquid crystal included roughly one quarter of the full die.

Wafer dicing and microprobing were performed on one of the failed die to try to isolate the cause of the faults. The die was depassivated and individual sub-circuits were isolated and tested. It was found during this process that the entire digital block was non-functional. The digital block had apparent over-current, failed communication logic, and failed logic input and output. The analog to digital converters incorporated into the ASIC were also non-functional. They relied heavily on the digital block, but this failed to explain an over-current measured on their separate filter power supply. In addition, low resistances were measured between several combinations of pins which should have been electrically isolated. One of these low resistance shorts was seen between a power supply trace (VBAT1) and a voltage regulator trace (VLDO). Another was observed between VLDO and the battery ground (VBAT0). It was not possible to isolate the location of these shorts by probing.

The probing and liquid crystal both showed strong evidence of a major defect in the digital block of the ASIC. Probing also revealed several low resistance shorts that liquid crystal was unable to detect due to insufficient power dissipation. Due to the complex and varied faults found in the die, localizing these faults using probing proved extremely difficult. Furthermore, the existence of many low-resistance shorts highlighted the shortcomings of liquid crystal. A global view of all the currents flowing through the device was requested by the design company to understand the overall behavior and specific fault locations of the device. To produce this current map, scanning magnetic microscopy [1-4] was employed.

Sample Preparation

Magnetic scanning was performed using Micro Magnetics' CS1000 scanning magnetic microscope. The ASIC was packaged in an open top ceramic leadless chip carrier (CLCC). The surface of the ASIC was 4 mm below the top of the LCC socket, and the total area of the die between the wirebonds, which surrounded the die on all sides, was 1.2 mm square. Because of these spatial constraints, scanning was performed using a standard vertical sensor probe using magnetic tunnel junction (MTJ) sensor technology. [5] This sensor probe tapers to a point and has a very small footprint (< 150 x 300 μ m), so that the sensor can be brought to within ~5 μ m of the sample surface even with limited access. A picture of the MTJ sensor probe is shown in Figure 1. Magnetic

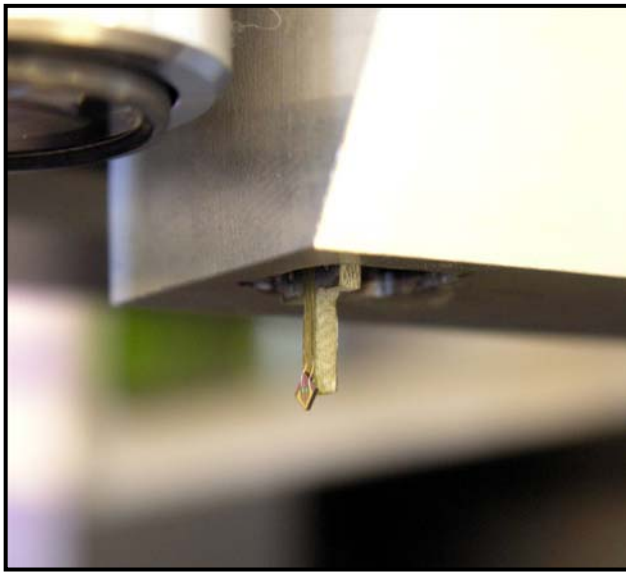


Figure 1. Picture of the MTJ vertical probe used for the magnetic current imaging case study.

scanning with MTJs can be done under ambient conditions, and no special preparation of the sample or the sensor probe was done. More details on the magnetic tunnel junction technology can be found following the case study.

Scanning was done in AC mode. In this mode, the CS1000 is only sensitive to the user specified modulation frequency, so no magnetic interference is possible. VBAT1 was powered with 2.3 V and the current was monitored by the system. A 300 mV peak-to-peak sine wave at 19 kHz was added on top of the DC supply voltage for imaging. This modulation voltage corresponded to $\sim 500 \mu\text{A}$ RMS of AC current.

Magnetic Scanning and Current Mapping

Because the die being imaged had been depassivated, scanning was done in a non-contact, plane-following mode to ensure that the sample would not be damaged. In this mode, the system uses a level sensor to automatically calculate the

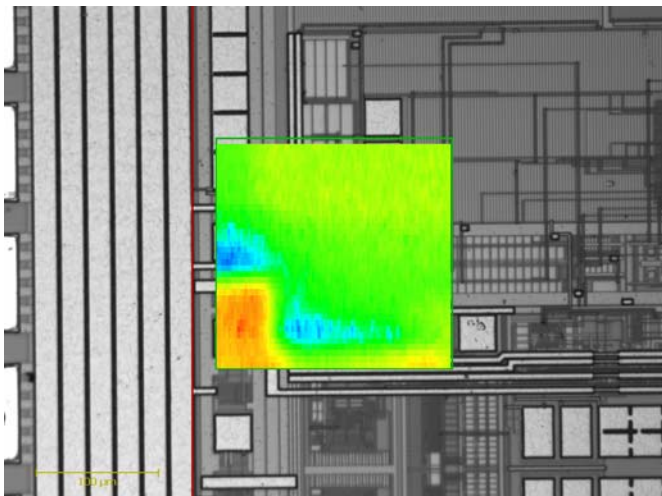


Figure 2. Magnetic field image confirming that current was entering the die through the VBAT1 wire bond, as expected.

tilt of the sample surface. The tilt is found by lowering the sensor probe onto the sample at a number of different positions on the die. Each time the sensor probe contacts the die, this level sensor automatically detects the contact force (the sensor is mounted on a very flexible assembly which keeps this force to $\sim 20 \mu\text{N}$ or less), immediately stops the motion of the sensor probe, and registers the location of the die surface to within $0.5 \mu\text{m}$. Once this procedure has been performed for five different locations on the die, the information collected is used to automatically calculate the tilt of the sample surface. During scanning, the system can then move the sensor probe vertically to maintain a constant distance ($\sim 5\text{-}10 \mu\text{m}$, in this case) between the probe and the die surface, without the need to physically level the die.

The MTJ mounted on the vertical probe was easily able to enter the cavity and contact the die. Regions of interest (ROIs) were selected visually by drawing rectangles on the optical or stitched image. The field of view of the optical camera with 10X objective which was used is $543 \times 408 \mu\text{m}$. To create the images of the full ($2 \times 2 \text{ mm}$) die the system captured and blended 16 optical images to create a stitched image. Conversion of the raw magnetic field data into maps of current density was accomplished using Micro Magnetics' Vista analysis package.

The first ROI to be magnetically imaged contained the current path between the VBAT1 wire bond and the point at which the current fans out into the die (Figure 2). Because this was the known point of entry of current onto the die, it was a logical starting point for tracing the current flow through the die. The current mapping proceeded to follow the VBAT1 current along its metal 3 trace across the die. The current on VBAT1 abruptly dropped to a perpendicular trace on metal 2. This was clearly an indication of a short between the VBAT1 metal 3 trace and the metal 2 trace below it. The rogue current is then seen looping into a section that completed the VBAT1 to VLDO current path, as shown in Figure 3. This was immediately identified as a major fault.

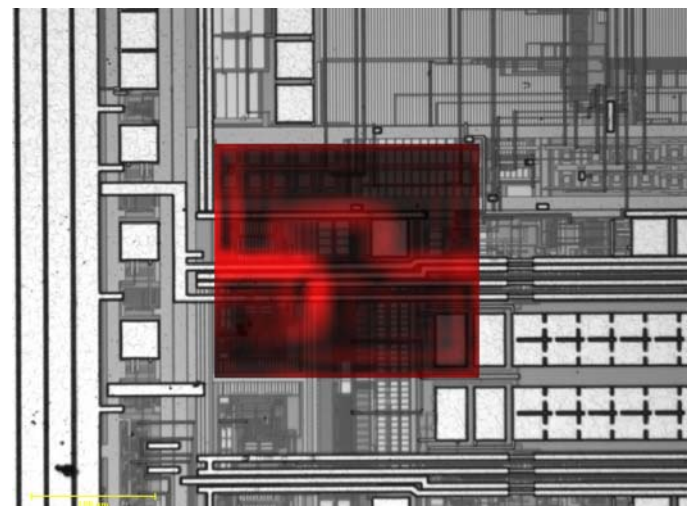


Figure 3. Current density image showing the flow of current through a short between the normally-open VBAT1 (M3) and VLDO (M2).

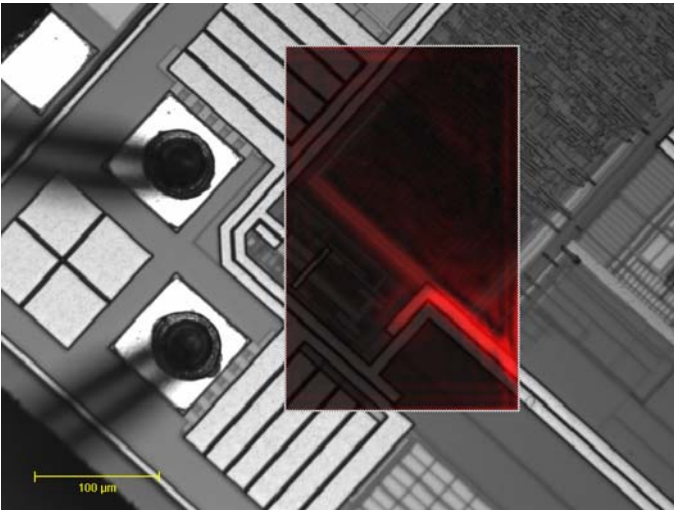


Figure 4. The current density map showing current entering the digital block.

The first images of this area showed the VLDO current path approaching the digital block along the expected path. As seen in Figure 4, these results show that the VBAT1 current approached the digital block along an interconnect on M4, taking a 90 degree left hand turn, passing through a via down a layer to a trace on M3, backtracking underneath its previous path, and then taking another 90 degree turn. After dropping down another layer and making more turns, the current continues along the edge of the digital block but then appears to disperse throughout the entire area immediately upon entering. This behavior was unexpected, because the assumption was that the current should have followed the VBAT1 trace around the digital block and to the VBAT0 trace. This indicated one or more shorts in the digital block, a result which made sense in light of the liquid crystal results.

Figure 5 shows a full-die current density map showing the path of the leakage current throughout the die.

Root Cause Isolation

The magnetic scanning results and associated optical image overlays had identified clear shorts in the die. The most obvious current path fault was imaged between the VBAT1 and the VLDO traces. These results also indicated a diffusion of current into the digital section of the die, which was likely the result of either multiple shorts or had been caused by some global problem in fabrication or processing.

To verify the current mapping results the faulty ASIC was imaged using scanning electron microscopy (SEM). High-magnification SEM images clearly showed metal whiskers in the VBAT1 to VLDO shorting area indicated by the current mapping. One such image is shown in Figure 6. However, the current path imaged with the CS1000, which showed shorting between metal layers, could not be directly isolated using the SEM without delayering the die. Further SEM images showed seemingly random metal whiskers throughout the die. The current leakage through the digital section was explained by the very dense network of interconnects this

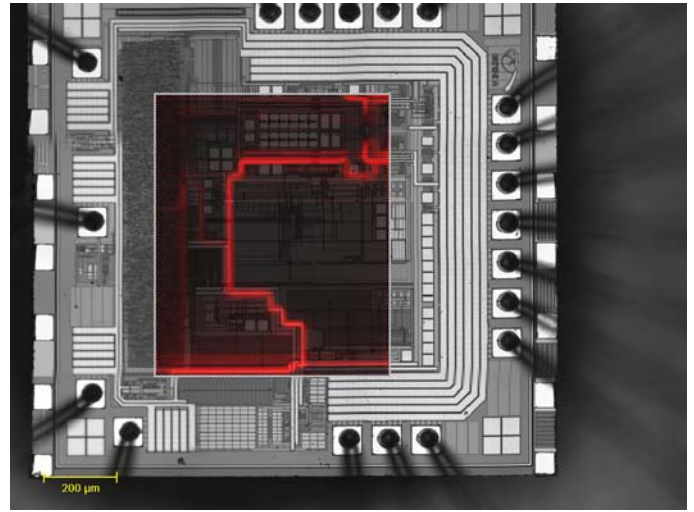


Figure 5. The overlaid full-die current density map shows the path of current through the die.

section being riddled with metal to metal shorts. Using the SEM, it was also noted that the observed track spacing between heavy metal traces was in violation of the design rules. The initial assumption of a design rule violation was thus corroborated. After consultation with the vendor, it was discovered that the vendor had accidentally disabled the specified track spacing rules during layout.

Discussion: Magnetic Tunnel Junction Sensors

Magnetic tunnel junction devices are thin film multilayer structures which were first experimentally realized in 1995. The core of a magnetic tunnel junction device is a tri-layer consisting of two magnetic films (electrodes) separated by an ultra-thin insulating layer. When a voltage is applied across this tri-layer, current can only traverse the structure via quantum mechanical tunneling. Due to the properties of the tunneling process, the resulting device has an electrical resistance which becomes dependent on the relative magnetic orientations of the two electrode layers. The performance on an MTJ device is often quantified by using the percentage change in resistance between the high-resistance and low-resistance states. This quantity is called the magnetoresistance

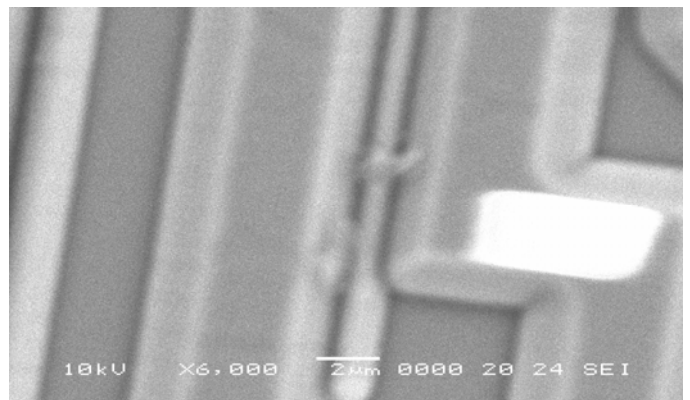


Figure 6. One of several SEM micrographs showing metal whiskers on the die. In this image, two whiskers are clearly seen near the center of the image.

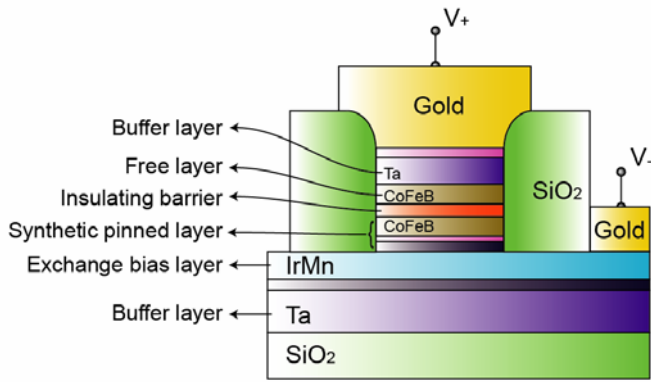


Figure 7. Schematic of the layer structure of the magnetic tunnel junction sensor device used for this study. The two electrodes are CoFeB, a material chosen for its favorable spin polarization, and the insulating barrier is MgO, which is key to realizing large magnetoresistance ratios.

of the device. Current MTJ sensors, such as the one used in the above case study, can have magnetoresistance ratios exceeding 200%, which allows them to easily beat the sensitivity of the more traditional giant magnetoresistance (GMR) or anisotropic magnetoresistance (AMR) sensors, which have magnetoresistances of 15-20% and 2-3%, respectively.

In order to translate this superior behavior into a useful device, several steps are taken. First of all, one of the two electrodes generally has its magnetization “pinned”. This is accomplished by a phenomenon called exchange bias which occurs when an antiferromagnetic material is deposited adjacent to this electrode. This layer is typically called the “pinned layer” of the structure and its magnetization remains fixed even in the presence of external fields of 500-1000 G or more. When the pinned layer’s magnetization is fixed in a particular direction, the device’s properties become suitable for use as a single bit of magnetic memory (this is the basis for most of the new magnetic random access memory – or

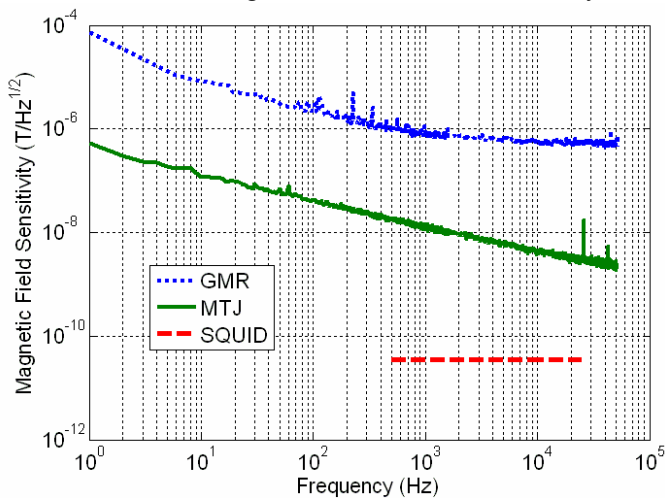


Figure 8. Magnetic field sensitivity data as a function of frequency for the three magnetic sensor technologies which have been used for magnetic current imaging.

MRAM– technologies). If the pinned layer’s magnetization is fixed in the perpendicular direction, the behavior of the device becomes linear, making it an excellent candidate for use as a low-field magnetic sensor. [5]

In order to create MTJ sensors with high spatial resolution, the MTJ film is patterned to microscopic dimensions using normal lithographic methods. In addition, the sensor’s resistance-versus-field response has been linearized. The details of all of these processes can be found elsewhere. In addition, several additional layers of material are added to the above structure for a variety of reasons. These include a “seed layer” deposited below the electrodes to promote smooth and epitaxial crystal growth, buffer layers above and below the structure to protect from physical damage, and a layer of gold so that the devices can be packaged using wire bonding. Figure 7 shows the full layer structure of the MTJ sensors used in this work.

Analysis: Comparison of Sensor Technologies

Three types of sensors have been reported as suitable for the purposes of magnetic current imaging: superconducting quantum interference device (SQUID) sensors [1,2], giant magnetoresistive (GMR) sensors [3,4,6], and magnetic tunnel junction (MTJ) sensors [3,5]. With magnetic current imaging, as with many other fault isolation techniques, sensitivity and spatial resolution are two of the most important figures of merit. In the following discussion, we will make direct comparisons between the performance of each type of sensor on the basis of sensitivity, spatial resolution, form factor, and other relevant parameters.

Magnetic and Current Density Sensitivity

The magnetic sensors used for magnetic current imaging techniques have sensitivities which are specified using units of magnetic field. In general, magnetic sensitivity (S_M) is frequency dependent and the sensitivity at a certain frequency is specified using units of $nT/Hz^{1/2}$. However, with regards to semiconductor applications, the most relevant quantity is actually the minimum detectable current (S_I , which would be specified using units of $nA/Hz^{1/2}$). Both of these related quantities are also frequency-dependent, and the latter is also distance-dependent. The values of magnetic sensitivity S_M are given for all three types of sensors, for frequencies from 1 to 50000 Hz, in Figure 8. In this figure, GMR and MTJ data are measured, while the SQUID numbers have been taken from previously published data [1]. The GMR sensor used for this study is a commercially-available device representative of those used for magnetic current imaging, while the MTJ sensor was a typical unit fabricated by Micro Magnetics. It should be noted that the magnetic field sensitivity of MTJ sensors further improves by an additional factor of 3-6 at higher frequencies, while GMR and SQUID sensors have already approached their white noise-limited sensitivity floor by 50 kHz. Because the amount of magnetic field created by a given amount

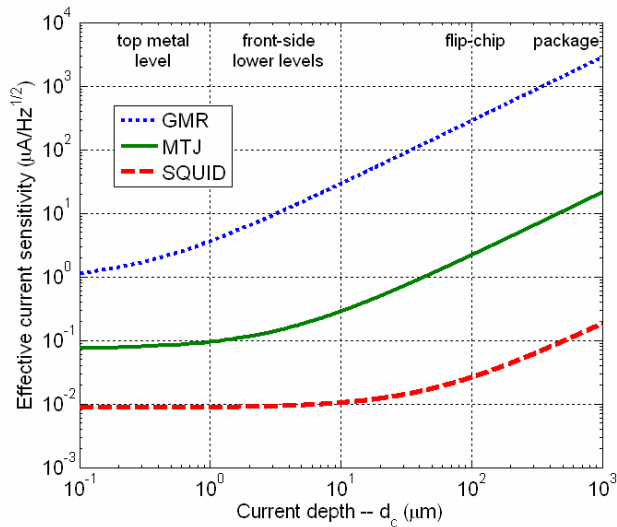


Figure 9. Effective current resolution for each type of sensor in units of $\mu\text{A}/\text{Hz}^{1/2}$, evaluated at 10000 Hz. Data are presented as a function of the sample-dependent distance between the sample surface and the current to be imaged.

of current is dependent both on its geometry and on how far away it is (and in some cases, on the geometry of the sensor), translating magnetic field sensitivity into current sensitivity requires some assumptions. Assuming the currents being imaged can be approximated by relatively long current paths, the current sensitivity is simply proportional to the magnetic sensitivity multiplied by the sensor-to-current distance z :

$$S_I = (2\pi / \mu_0) S_M z$$

(Because a smaller S_I indicates a better sensitivity, a minimal distance between sensor and current leads to better sensitivity). The distance between the sensor and the current (z) can be expressed as the sum of two terms: 1) the sensor-dependent distance (d_S) between the sensor active area and the physical bottom of the sensor, and 2) the sample-dependent distance (d_c) between the surface of the sample and the current density to be imaged. The latter of the above terms is independent of the choice of magnetic sensor, so for the purposes of comparison, we will focus on only the first term. Figure 9 compares the current sensitivity, evaluated at 10000 Hz, for all three types of sensors.

Because the definitions of spatial resolution and sensitivity above both depend on the sample-dependent distance between the surface of the device and the actual current flow (denoted d_c), Figure 9 plots the current sensitivity as a function of this parameter. This figure covers the full range of d_c values expected for different types of samples. For example, a front-side structure where the current is very close to the surface of the sample might have $d_c = 1 \mu\text{m}$. A front-side device with many intervening metal layers or a thick passivation would be in the neighborhood of $d_c = 10 \mu\text{m}$. Finally, a thinned flip-chip might feature $d_c = 80\text{-}150 \mu\text{m}$ while imaging a package would likely result in a value of $d_c = 200\text{-}1000 \mu\text{m}$. It is important to note that these values assume that the sensor probe can be brought very close to the sample surface. If this

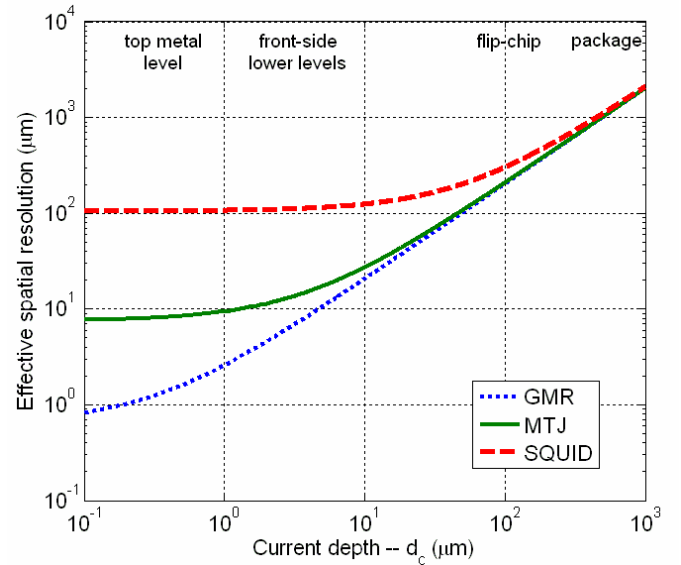


Figure 10. Effective figure-of-merit for sensor spatial resolution as a function of the sample-dependent distance between the sample surface and the current to be imaged.

is not possible (i.e. physical obstructions such as wirebonds preventing the sensor from approaching), the effective value of d_c will be larger.

Spatial Resolution

Spatial resolution in magnetic current imaging is even more difficult to cleanly define. It can be defined as the minimum spacing between two parallel current paths for which they can still be individually resolved, or as the precision with which the position of a current path can be specified. Or, alternatively, it can be defined as size of the smallest defect of a given type which can be located from the current density map. While no single definition of spatial resolution can fully describe all situations, it is the case that the spatial resolution of the technique, by most definitions, will be dependent on the distance between the sensor and the current path, and in some cases on the geometry (active area) of the sensor itself. Quantifying this, one good figure-of-merit for the spatial resolution (d_s) of a given sensor is

$$\sqrt{(2z)^2 + w^2}$$

where z is (again) the sensor-to-current distance and w is the lateral dimension of the sensor's active area. The actual spatial resolution of the technique is generally equal to some constant multiplied by the above expression, where the constant depends on the definition of resolution which is used. However, for the purposes of comparing sensors, the above expression is quite useful.

Figure 10 shows the overall figure-of-merit for spatial resolution for both GMR and MTJ sensors for each of these cases, again presented as a function of the sample-dependent current depth d_c . This figure shows that for samples with deep currents (packages, unpolished flip-chips) the spatial

Sensor Type	Field Sensitivity @ 10 kHz	Current Sensitivity @ 10 kHz, $d_c = 1 \mu\text{m}$	Current Sensitivity @ white-noise	Intrinsic Spatial Resolution	Sensor Geometry	Sensor Footprint Area
	(nT/Hz ^{1/2})	($\mu\text{A}/\text{Hz}^{1/2}$)	($\mu\text{A}/\text{Hz}^{1/2}$)	$0.5d_s$ (μm)		(mm ²)
GMR	560	3.6	2.6	0.3	Horizontal cantilever	1.25
MTJ	4.2	0.09	0.02	3.8	Tapered vertical probe	0.045
SQUID	0.035	0.009	0.009	53	Vertical cylinder	3.14

Table I. Comparison of key parameters for the three types of sensors. Current sensitivity values assume $d_c = 1 \mu\text{m}$. SQUID sensor footprint is estimated from [6].

resolution of all sensors approaches the same value, while for currents within $\sim 30 \mu\text{m}$ of the surface, there is a sizable advantage for GMR and MTJ sensors in terms of spatial resolution.

Sensor Geometry and Footprint

Another consideration important in selecting a sensor is its footprint and physical orientation. Each of the three sensor technologies has a different geometry and footprint, which may in some cases restrict their use in some types of samples, particularly those with recessed surfaces, those requiring powering by microprobes, or samples with wire bonds in close proximity to the region of interest. Figure 11 shows a comparison of sensor form factors and footprints for the three types of sensors.

Based on the most recent published work, the SQUID sensor used for magnetic current imaging [6] is a tapered cone which

comes to a circular footprint which is more than 1.5 mm across. Because a very thin window separates the cryogenic SQUID sensor from the room-temperature sample, these sensors can only be safely utilized in non-contact mode. GMR sensors have a rectangular footprint of 1.25 x 1.0 mm, and must be scanned in contact with the sample in order to realize their primary advantage of high spatial resolution. However, GMR sensors come on a cantilever which extends almost horizontally, making accessing some devices more difficult. MTJ sensors have a vertical probe geometry, with a thin probe that tapers at a 45° angle, and can be used for contact-mode or non-contact-mode scanning. The tapered geometry creates a much smaller footprint of $\sim 0.15 \times 0.3 \text{ mm}$. Because the sample used for the above case study had a total area between wire bonds of just over 1 mm², the MTJ sensor was the only one which would have been suitable for this work.

Discussion

A full summary of the various parameters of interest are listed for each sensor in Table I.

From Figures 9 and 10, it is clear that the best choice of sensors is highly dependent on how close the sensor's active area can be brought with respect to the currents to be imaged (d_c). For samples with $d_c < 20 \mu\text{m}$, the MTJ and GMR sensors offer big advantages in terms of spatial resolution, and for very small values of d_c , the current sensitivity of these sensors actually makes significant gains versus the SQUID (with the MTJ's current sensitivity making significant gains versus that of the SQUID for $d_c \sim 1 \mu\text{m}$). However, for samples with $d_c > 100 \mu\text{m}$, the SQUID's higher sensitivity is the deciding factor, as the spatial resolution of the three sensors begins to approach the same sample-limited value in this case. One interesting conclusion that can be made is that only for very small values of d_c does the high spatial resolution of GMR devices give them a significant advantage over MTJ sensors,

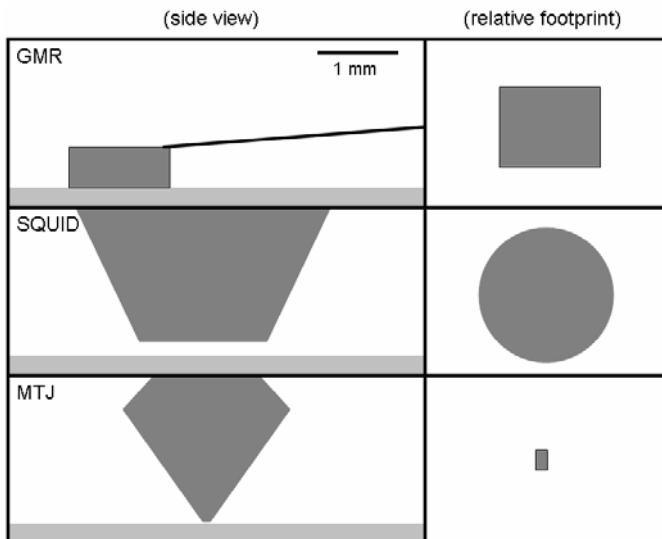


Figure 11. Comparison of the three types of sensors in terms of geometry (left) and footprint (right).

which have a much higher current sensitivity over the full range of d_c values.

Finally we note that MTJ sensors have noise characteristics dependent on the size of the active area of the sensor. The limiting noise at Hz-kHz frequencies, which is $1/f$ in nature (see Figure 8), scales as the inverse of the square-root of the sensor volume. This allows the spatial resolution of an MTJ sensor to be traded-off for increased sensitivity, by increasing the lithographically-defined size of the sensor element. While similar relationships between sensitivity and resolution hold for SQUID and GMR sensors, neither of these sensor technologies currently allows the user to make this type of trade-off. Although it has not been demonstrated, it is estimated that increasing the size of an MTJ sensor to that of the SQUID sensor should result in a three- to five-fold improvement in current and field sensitivity. This would be useful, for example, for imaging samples with deep current paths (i.e. packages), where a small sensor volume is not critical.

References

1. S. Chatrathorn, E. F. Fleet, F. C. Wellstood, L. A. Knauss, and T. M. Eiles, *Scanning SQUID microscopy of integrated circuits*, *Appl. Phys. Lett.*, 76, 2304 (2000).
2. D. P. Vallett, *Scanning SQUID Microscopy for Die Level Fault Isolation*, *Proc. 28th Int. Symp. for Test. and Failure Analysis (ISTFA)*, Nov. 2002.
3. B. D. Schrag, M. J. Carter, X. Y. Liu, and Gang Xiao, *Scanning magnetoresistive microscopy for die-level sub-micron current density mapping*, *Proc. 29th Int. Symp. Test. and Failure Analysis (ISTFA)*, Nov. 2003.
4. B. D. Schrag, Xiaoyong Liu, J. S. Hoftun, P. L. Klinger, T. M. Levin, and D. P. Vallett, *Quantitative Analysis and Depth Measurement via Magnetic Field Imaging*, *EDFA Magazine*, Nov. 2005.
5. Xiaoyong Liu, C. Ren, and Gang Xiao, *Magnetic tunnel junction sensors with hard-axis bias field*, *J. Appl. Phys.* 92, 4722 (2002).
6. S. I. Woods, Nesco M. Lettsome Jr., A. B. Cawthorne, L. A. Knauss, and R. H. Koch, *High Resolution Current Imaging by Direct Magnetic Field Sensing*, *Proc. 29th Int. Symp. Test. and Failure Analysis (ISTFA)*, Nov. 2003.